Superabsorbing Metasurfaces with Hybrid Ag–Au Nanostructures for Surface-Enhanced Raman Spectroscopy Sensing of Drugs and Chemicals

Jun Gao, Nan Zhang, Dengxin Ji, Haomin Song, Youhai Liu, Lyu Zhou, Zhi Sun, Josep M. Jornet, Alexis C. Thompson, R. Lorraine Collins, Yun Song,* Suhua Jiang, and Qiaoqiang Gan*

Dedicated to the memory of Dr. Suhua Jiang (1976–2017)

Reliability, shelf time, and uniformity are major challenges for most metallic nanostructures for surface-enhanced Raman spectroscopy (SERS). Due to the randomness of the localized field supported by silver and gold nanopatterns in conventional structures, the quantitative analysis of the target in the practical application of SERS sensing is a challenge. Here, a superabsorbing metasurface with hybrid Ag–Au nanostructures is proposed. A two-step process of deposition plus subsequent thermal annealing is developed to shrink the gap among the metallic nanoparticles with no top-down lithography technology involved. Because of the light trapping strategy enabled by the hybrid Ag–Au metasurface structure, the excitation laser energy can be localized at the edges of the nanoparticles more efficiently, resulting in enhanced sensing resolution. Intriguingly, because more hot spots are excited over a given area with higher density of small nanoparticles, the spatial distribution of the localized field is more uniform, resulting in superior performance for potential quantitative sensing of drugs (i.e., cocaine) and chemicals (i.e., molecules with thiol groups in this report). Furthermore, the final coating of the second Au nanoparticle layer improves the reliability of the chip, which is demonstrated effective after 12 month shelf time in an ambient storage environment.

1. Introduction

Surface-enhanced Raman spectroscopy (SERS) refers to a powerful vibrational spectroscopic technique capable of enhancing the weak and inelastic Raman scattering of low concentration analytes bound to, or near patterned metallic surfaces.[1,2] Utilizing this sensitive sensing technology, glucose, oligonucleotides, explosives, and other analytes of interest have been detected.[3,4] In recent years, the unprecedented ability of nanoplasmonic/metamaterial structures to concentrate light has attracted significant research interests.[5] It has been reported that the optical field can be concentrated into deep-subwavelength volumes and realize significant localized-field enhancement (so called hot spot) using a variety of nanostructures (e.g., nanoparticle/sphere array, bow-tie nanoantennas, and nanorods).[6,7] More specifically, plasmonic nanostructures with highly controlled ultrasmall nanogaps can generate stronger SERS signals from molecules in the nanogap.[8,9] However, due

J. Gao, Prof. Y. Song, Prof. S. Jiang[†]
Department of Materials Science
Fudan University
Shanghai 200433, China
E-mail: songyun@fudan.edu.cn
N. Zhang, Dr. D. Ji, Dr. H. Song, Y. Liu, L. Zhou, Prof. Z. Sun,
Prof. J. M. Jornet, Prof. Q. Gan
Department of Electrical Engineering
University at Buffalo
The State University of New York
Buffalo, NY 14260, USA
E-mail: qqgan@buffalo.edu

[†]Deceased December 31, 2017.

Prof. A. C. Thompson
Research Institute on Addictions, University at Buffalo
The State University of New York
Buffalo, NY 14203, USA

Prof. R. L. Collins
Department of Community Health and Health Behavior
University at Buffalo
The State University of New York
Buffalo, NY 14214, USA

**ADVANCED
SCIENCE NEWS**

www.advancedsciencenews.com

**small
methods**

www.small-methods.com

to the diffraction limit of conventional optics, the light coupling efficiency from free space into deep-subwavelength volumes is usually very weak. Furthermore, current dominant fabrication techniques (e.g., electron beam (e-beam) lithography, nanoimprint, self-assembled nanosphere, hybrid nanoporous lithography methods) are expensive and complicated to fabricate high quality SERS substrates over large areas, thus resulting in high prices for commercial SERS substrates (e.g., refs. [10–13]). To overcome these limitations, recently we developed a simple, low-cost, scalable, and lithography-free method to manufacture three-layered metal–dielectric–metal (MDM) metamaterial superabsorbers for SERS sensing.[14,15] Using direct deposition and post-thermal annealing processes, superabsorbing plasmonic metamaterial structures were created with very broad light trapping bands (i.e., >80% absorption band from 414 to 956 nm[16]). In particular, the incident light can be efficiently coupled into the three-layered structure and localized at edges of nanoparticles (NPs), enabling the surface-enhanced light–matter interaction for SERS. More importantly, this efficient light trapping metasurface structure is completely lithography free, suitable for large area manufacturing including roll-to-roll processes. It will enable the development of low-cost high-performance SERS chips for the emerging portable Raman spectroscopy systems.

In general, gold (Au) and silver (Ag) are the most popular materials for SERS substrates. Au NPs are stable and biocompatible with various biomolecules like antigen, antibody, and DNA.[17] Usually, Ag nanostructures exhibit better performance in SERS due to the stronger localized field. However, because of the surface oxidization, Ag nanostructures are less stable with shorter operational lifetime (i.e., shelf time). Therefore, most commercial SERS products are based on Au nanostructures (e.g., gold nanopillars[18] and gold nanopatterns[19]). Recently, Au@Ag core–shell NPs and Au/Ag alloy nanocomposites were proposed to realize better performance in SERS applications with improved stability.[20,21] In this work, we report a three-layered metamaterial superabsorber structure with hybrid random Au and Ag NPs as the top layer. By immobilizing smaller Au NPs between larger Ag NPs, the gap between metallic NPs can be reduced significantly. Smaller gaps will result in stronger localized field due to optically driven free electrons coupled across the gap, and, therefore, boost the SERS sensing performance. In addition, due to the better stability of Au NPs and larger density of molecules on Au surfaces, the proposed hybrid Ag–Au metasurface is promising to enable better sensing of biomolecules. Since no top-down lithography procedures were involved in the fabrication (e.g., electron beam lithography, nanoimprint, focused-ion-beam, and self-assembled nanosphere methods[10–13]), the proposed hybrid Ag–Au superabsorber metasurface is promising to realize a high performance, broadband, and inexpensive sensing chip for SERS applications.

## 2. Results and Discussion

2.1. Nanofabrication

Figure 1a–c illustrated the fabrication procedure: the three-layered superabsorbing metasurface is composed of a 150 nm thick Ag ground plate, a 50 nm thick aluminum oxide (Al_2O_3) spacer layer, and a layer of random metallic NPs. We first deposited a layer of

Ag and Al_2O_3 spacer on a glass substrate (Figure 1a). Following our previously reported lithography-free fabrication technique,[14] direct deposition of Ag followed by thermal annealing was used to manipulate the average morphology (e.g., size, spacing) of the first layer of Ag NPs (Figure 1b) to tune the effective optical constant and realize the desired light-trapping band (see more details in the Experimental Section). Next, a second Au film with the thickness of 5 nm was deposited on top of Ag NPs. The substrate was then annealed at 150 °C to further manipulate the NP size and interparticle distance of Au NPs (Figure 1c). This second step deposition and low temperature thermal annealing did not obviously change the morphology of the first layer Ag NPs treated under higher temperature. As shown by the scanning electronic microscope (SEM) image of the three-layered metafilm at a tilted angle (Figure 1d), the second layer Au NPs were placed among the first layer of Ag NPs to shrink the nanogap.

The optical absorption of the hybrid Ag–Au metasurface was characterized using a microscopic Fourier transform infrared spectroscopy (Bruker, VETEX 70 + Hyperion 1000). A strong absorption peak of 98.7% was obtained at the wavelength of 900 nm with the >90% absorption band spanning from 784 to 1030 nm (see the red curve in Figure 1e), significantly broader than previously reported results (e.g., refs. [22,23]). This is due to the nanocavity-induced absorption enhancement with engineered optical constants, as we reported in refs. [24–26]. By changing the shapes of randomly distributed NPs deposited under different conditions, the effective optical constants of surface nanoparticle layer can be tuned to control the bandwidth and amplitude of the absorption of the three-layered nanocavity structure. Compared with the metasurface without the second-step process (see the yellow curve in Figure 1e), one can see a redshift in the absorption peak from 725 to 900 nm due to the change in thin film interference conditions.[24,25] In addition, a single layer of Ag NPs and a single layer of Ag–Au NPs on glass substrates were prepared as reference samples in the same film deposition and thermal annealing conditions. Their optical absorption spectra are plotted by the green and purple curves in Figure 1e, showing only 29–42% throughout the measured spectral range. Based on this experimental characterization, one can see that after the second-step fabrication process, the metasurface structure still preserves the broadband light trapping feature with slightly shifted resonant wavelengths. These smaller gaps are promising to obtain stronger localized field, which is highly desired for enhanced light–matter interaction (e.g., SERS and surface-enhanced nonlinear optics[26]), as will be discussed below.

2.2. Structure Characterization

To reveal the field localization feature, we focused on the wavelength at the intersection point between two absorption curves (see the black arrow in Figure 1e). At this wavelength (≈785 nm), the overall optical absorption of these two samples are similar (i.e., ≈90%). However, since the hybrid Ag–Au metasurface sample contains smaller gaps, more hot spots are expected with stronger localized field. To validate this prediction, we loaded a part of the SEM image of the top films shown in **Figure 2**a,b (i.e., the white dotted squares) into the commercial software package, COMSOL, and modeled the spatial distribution of
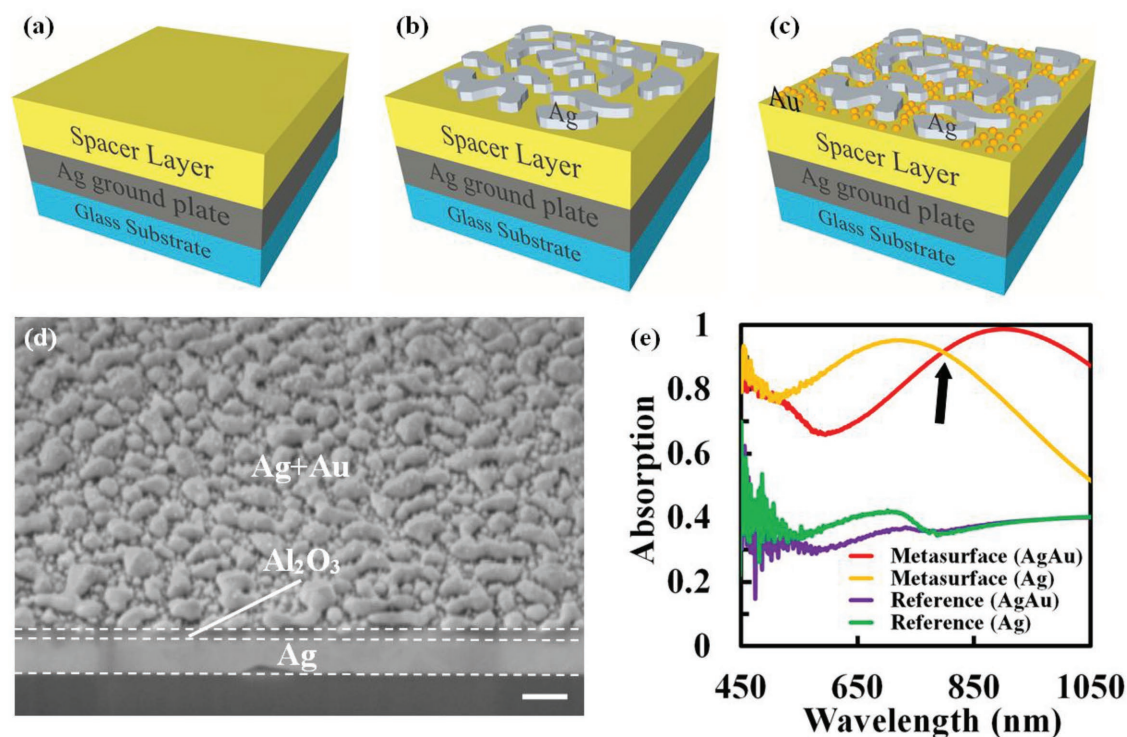
Figure 1. a–c) Manufacturing procedure to fabricate three-layered absorbing metasurface with multistep deposition processes. d) A tilted cross-sectional SEM image of three-layered absorbing metasurface on silicon substrate. Scale bar: 200 nm. e) Absorption spectra of the three-layered absorber before (yellow curve) and after (red curve) the second-step deposition, and their corresponding reference structures with NPs only on glass substrates (green and purple curves).

the electric field at λ = 785 nm. As shown in Figure 2c,d, the coverage area of hot spots increased from 13.6% to 21.6% (i.e., enhanced by 58.8%). More hot spots are obtained between large and small NPs, enabling more sensing areas with stronger localized field, which is highly desired for SERS sensing.

To demonstrate the localized field enhancement, we then employed this hybrid Ag–Au superabsorbing metasurface in

detecting 1,2-bis(4-pyridyl)-ethylene (BPE) molecules. Since BPE molecules include a highly delocalized π-electron system with chemically active pyridyl nitrogen atoms for binding to metal surfaces, they have been widely used as stable non-resonant probing molecules to evaluate the performance of SERS substrates and reveal the localized field enhancement effect (e.g., refs. [27,28]). In this experiment, two metasurfaces
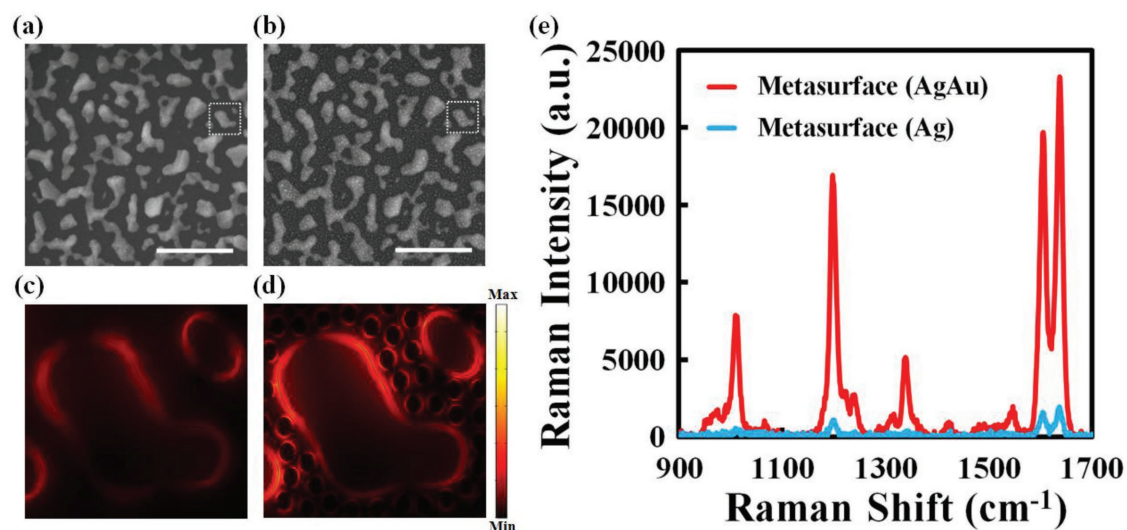
Figure 2. a,b) SEM images of top random Ag NPs (a) before and (b) after an extra 5 nm thick Au NP deposition. The scale bar is 500 nm. White dotted squares: areas loaded for simulation. c,d) Modeled electric field enhancement distribution among the NPs (at λ = 785 nm) in the white dotted squares in (a) and (b) at the normal incidence. e) SERS spectra of BPE molecules on metasurface chips with and without the second-step deposition process.

1800045 (3 of 9)

without and with the second-step deposition process were both immersed in 1×10^{-3} M BPE ethanolic solutions for 10 min and then air-dried. Next, they were rinsed with pure ethanol. The SERS signals of these two samples were characterized using a benchtop confocal Renishaw inVia Raman microscope equipped with a 785 nm laser. As shown in Figure 2e, obvious Raman peaks at 1012, 1200, 1340, 1608, and 1637 cm^{-1} were observed, which are signature "fingerprint" signals for BPE molecules. One can see that the Raman signal from the hybrid Ag–Au metasurface is much stronger than the metasurface with Ag NPs only, demonstrating the stronger electric field introduced by smaller gaps. Using this result, one can estimate the enhancement factor (EF) of both SERS metasurfaces without and with the second-step deposition process to be 4.7×10^6 and 7.3×10^7, respectively (see more details on enhancement factor calculation in the Experimental Section). Considering that the overall optical absorption of these two samples are similar (i.e., ≈90%), it indicates the further enhanced light–matter interaction by introducing smaller gaps over a large area.

2.3. Spatial Uniformity

As demonstrated in Figure 2c,d, these hot spots supported by smaller gaps distribute more uniformly compared with the one with no second-step NPs. Therefore, the hybrid Ag–Au superabsorbing metasurface with smaller gaps is promising to result in better spatial uniformity. In this experiment, a 2D Raman mapping at the peak of 1608 cm^{-1} was performed over a 30 µm × 30 µm area with a step size of 1 µm. The relative standard deviations of Raman intensities of metasurfaces without (**Figure 3**a) and with (Figure 3b) the second-step deposition process are 8.14% and 5.89%, respectively, confirming the improved spatial uniformity introduced by the second-step

NPs. This uniformity is only slightly lower than those SERS substrates with periodic patterns fabricated by expensive lithography methods (e.g., 5%[29]) and is promising to enable affordable quantitative analysis. Realization of high resolution quantitative sensing via cost-effective chips is one of the grand challenges for SERS sensing.[30] To evaluate the limit of detection of our metasurface chips, we placed 10 µL BPE ethanolic solutions onto the metasurface chips with the concentrations from 1×10^{-3} M to 100×10^{-9} M, then air-dried these chips. Figure 3c exhibits the SERS spectra of BPE solutions with different concentrations. The signature Raman peaks of BPE were observable at concentrations as low as 100×10^{-9} M. By extracting the signal peak intensities at the specific Raman peak at 1608 cm^{-1}, one can reveal its linear relationship with the concentration of BPE ethanolic solution. As shown by the data fitting of the signal intensity at a selected peak at 1608 cm^{-1} in Figure 3d, a linear correlation coefficient of 0.983 is achieved, suggesting its potential for quantitative SERS analysis (the fittings to other peaks are shown in Section S1 in the Supporting Information).

2.4. Shelf Time

In practical applications (especially for commercial SERS chips), shelf time is usually an important parameter: due to the fragile nanostructure and stability of metal materials (e.g., Ag), the claimed shelf time for most commercial SERS chips is relatively short. The performance of SERS chip may degrade over time, especially for Ag-based structures. For instance, the SERS intensity of silver nanorod substrates dropped nearly 80% after one week of storage in ambient environment (see cyan dotted curves in Figure 3e).[31] For our proposed hybrid Ag–Au metasurface chip, the second layer of Au NPs covers the entire
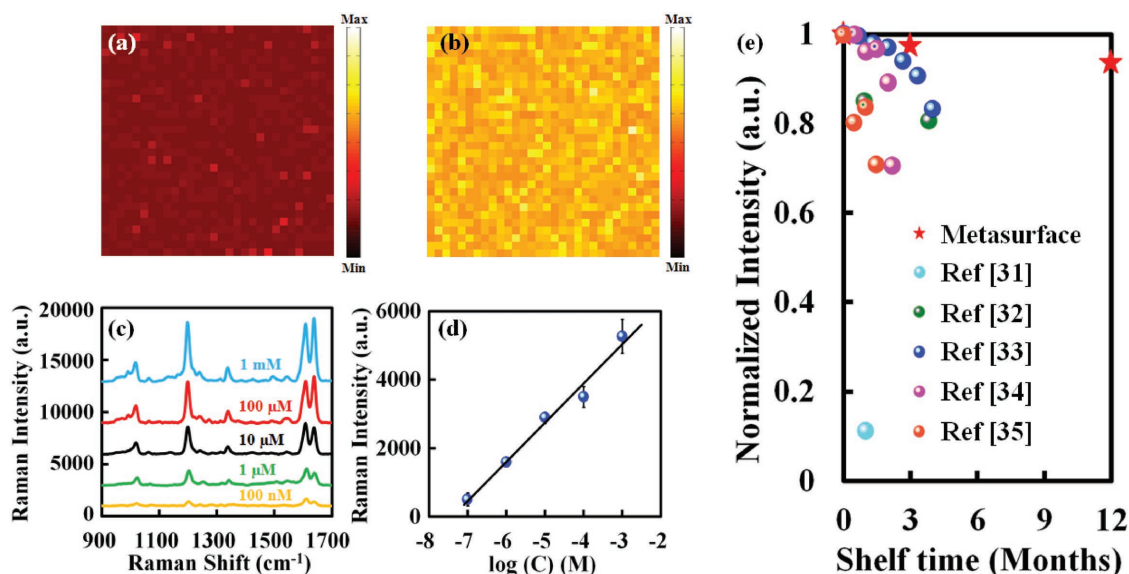

Figure 3. a,b) Raman maps of metasurfaces (a) without and (b) with the second-step deposition process within an area of 30 µm × 30 µm. c) SERS spectra of BPE ethanolic solutions with different concentrations on the hybrid Ag–Au metasurface. d) Relationship between the Raman intensities at the peak of 1608 cm^{-1} and different concentrations of BPE ethanolic solutions. e) Direct comparison of Raman intensities over different periods obtained by previously reported structures (data from refs. [31–35]) and the metasurface (i.e., the red stars).

surface, including the larger Ag islands (Figure 2b). Therefore, the oxidization of Ag surface was suppressed. In addition, as shown in Figure 2d, more hot spots were localized at edges of Au NPs, while the overall light trapping performance did not change significantly (see Section S2 in the Supporting Information). Therefore, the oxidization of Ag NP surfaces will not significantly affect the performance in SERS sensing. To reveal the shelf time of our proposed structure, we stored the sample in an ambient laboratory environment with the ambient temperature of 20–23 °C and the humidity between 20% and 60%. To test its shelf time, we prepared 1×10^{-3} M BPE ethanolic solutions and followed the same sample preparation procedure to perform the characterization after 3 and 12 month storage. As shown in Figure 3e, the degradation rate of the peak intensity at 1608 cm^{-1} is less than 10%, which is much better than previously reported nanostructures (see data captured from refs. [31–35] in Figure 3e). This comparison demonstrated that the proposed Ag–Au metasurface stayed effective after one year shelf time in an ambient storage environment. The final coating of the second Au NPs layer improved the reliability of the chip. It should be noted that ref.[33] demonstrated a thin-layer chromatography plate with Au NPs. The relative standard deviation of the SERS performance was less than 16%. In ref. [35], the spot-to-spot change in SERS intensity of reported Au/WO$_3$/TiO$_2$ nanosheets was less than 15%. In contrast, the relative standard deviation of our hybrid Ag–Au metasurface is less than 6%, much better than those structures both in shelf time and uniformity.

2.5. Application

To demonstrate the practical application of the proposed hybrid metasurface SERS chip, we first selected cocaine as the sensing target. Cocaine is one of the most important drugs related to forensic analysis (e.g., ref. [36]). The widespread abuse of illicit drugs (e.g., cocaine, heroin, amphetamines, hallucinogens) is a growing societal problem in the United States and many other countries (e.g., ref. [37]). In clinical and forensic trace analysis, there is a great need to develop a sensitive, reliable, and fast sensing technology. In order to evaluate the limit of detection of the hybrid Ag–Au metasurface for drug sensing and potential forensic analysis, a series of low-concentration cocaine solutions were tested. In the experiment, we placed 10 µL cocaine acetonitrile solutions onto the metasurface chips with the concentrations from 100 to 1 µg mL^{-1}, then air-dried these chips. As shown in **Figure 4**a, the vibrational modes of the cocaine molecules can be identified from the Raman spectra:[38] the signature Raman peaks of cocaine at 1001 cm^{-1} (i.e., the symmetric phenyl ring breathing mode), 1027 cm^{-1} (i.e., the asymmetric phenyl ring breathing mode), 1275 cm^{-1} (i.e., the C−phenyl stretch), and 1598 cm^{-1} (i.e., the trigonal phenyl ring breathing mode) are observable at concentrations as low as 10 µg mL^{-1}. Considering the droplet volume of 10 µL and the coverage area of ≈20 mm^2 on the metasurface, the averaged density of cocaine on the metasurface was only 5 ng mm^{-2}, which is much better than previously reported results (e.g., 200 ng mm^{-2},[39] ≈446 ng mm^{-2},[40] 314 ng mm^{-2},[41] and 1900 ng mm^{-2}[42]). For
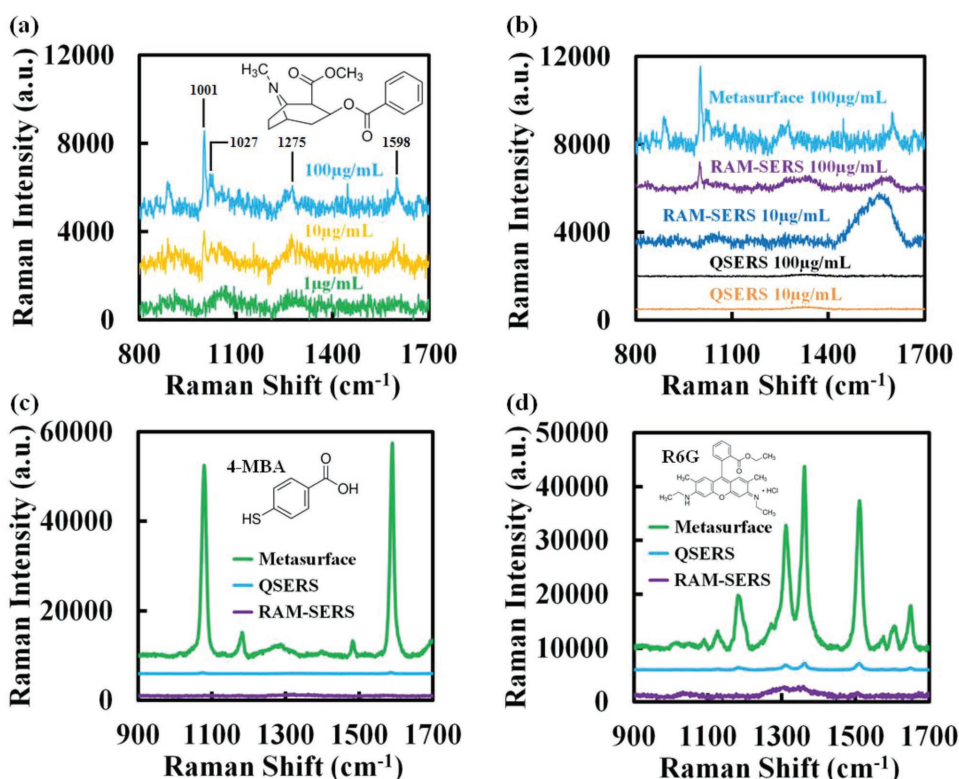
Figure 4. a,b) SERS spectra of cocaine acetonitrile solutions with different concentrations on (a) the hybrid Ag–Au metasurface and (b) two commercial substrates. Inset in (a): chemical structures of cocaine molecule. c,d) SERS spectra of (c) 4-MBA and (d) R6G molecules on the hybrid Ag–Au metasurfaces and two commercial substrates. Insets: chemical structures of (c) 4-MBA and (d) R6G molecules.

better comparison, two commercial substrates (i.e., QSERS and RAM-SERS) were prepared under the same procedure and measured using identical experimental conditions, as shown in Figure 4b. One can see that only the concentration of 100 µg mL^{-1} can be observed using the commercial RAM-SERS substrate. The other commercial chip, QSERS substrate, cannot detect these cocaine solutions.

In addition, another two widely used chemical molecules (i.e., 4-mercaptobenzoic acid (4-MBA) and rhodamine 6G (R6G)) were also tested on these chips. In the experiment, we placed 1 µL 4-MBA ethanolic solutions and R6G aqueous solutions (with the concentrations of 1×10^{-3} M) onto the metasurface chips and two commercial substrates, then air-dried these chips. As shown in Figure 4c, the vibrational modes of the 4-MBA molecules were observed clearly on our metasurface chip, corresponding to the v(C—C) stretch mode and aromatic ring breathing mode.[43,44] In contrast, almost no signals can be observed from those two commercial products. For R6G molecules, as shown in Figure 4d, the vibrational modes at 1185, 1311, 1361, 1511, 1649 cm^{-1} correspond to C—H in-plane bending, C—O—C stretching, and C—C stretching of aromatic ring modes.[45] One can see that the Raman signal from the hybrid Ag–Au metasurface is 29 times stronger than the commercial QSERS substrate at the peak of 1361 cm^{-1}. The other commercial chip, RAM-SERS substrate, cannot detect these R6G solutions. This experiment clearly demonstrated the improved sensing performance of the proposed hybrid Ag–Au metasurface chip with smaller nanogaps.

Finally, we further explored the superior sensing capability based on surface chemical properties of Au and Ag NPs. For instance, it is known that the thiol−Au chemical binding is much stronger than the thiol−Ag binding (e.g., refs. [46,47]). The thiol group is a typical group of chemical molecules

containing a sulfur atom and a hydrogen atom (i.e., −SH). In surface treatment of substrates for many bio/chemical investigations, thiol functional group molecules are widely used as building blocks (e.g., ref. [48]). In addition, the detection and measurement of free thiols (e.g, free cysteine, glutathione, and cysteine residues on proteins) is one of the essential tasks for investigating biological processes and events in many biological systems. Therefore, the proposed hybrid Ag–Au metasurface structure is promising to realize unique sensing capabilities for specific bio/chemical molecules with thiol groups.

To demonstrate the potential enhancement effect of Au−S binding, in this experiment, we employed benzenethiol (BZT) molecules as the probe and developed three different metasurface chips for comparison. BZT is one of the simplest aromatic thiols with four obvious Raman peaks at 1000, 1022, 1076, and 1576 cm^{-1} which are easy to recognize. When BZT molecules adsorb to the nanostructured chip, the sulfur atoms are strongly bounded to the metal surface and form benzenethiolate.[49] To ensure a complete self-assembled monolayer (SAM) of BZT formed on the substrate surface, three metasurface substrates were immersed in 100×10^{-6} M BZT ethanolic solutions for 1 h and were subsequently rinsed with pure ethanol before air-drying. In this experiment, three metasurface chips without and with the second-step NPs deposition process were fabricated: i.e., single-Ag, Ag–Ag, and Ag–Au metasurface chips. These three types of structures were fabricated starting from the same first-step deposition of Ag nanopatterns. Next, the second layer of Ag film and Au film with the same thicknesses (i.e., 5 nm) were deposited on top of the first layer Ag NPs, respectively. Then, both the substrates were annealed at 150 °C to adjust NP sizes and interparticle distances. Their optical absorption spectra are plotted in **Figure 5**a, showing that all
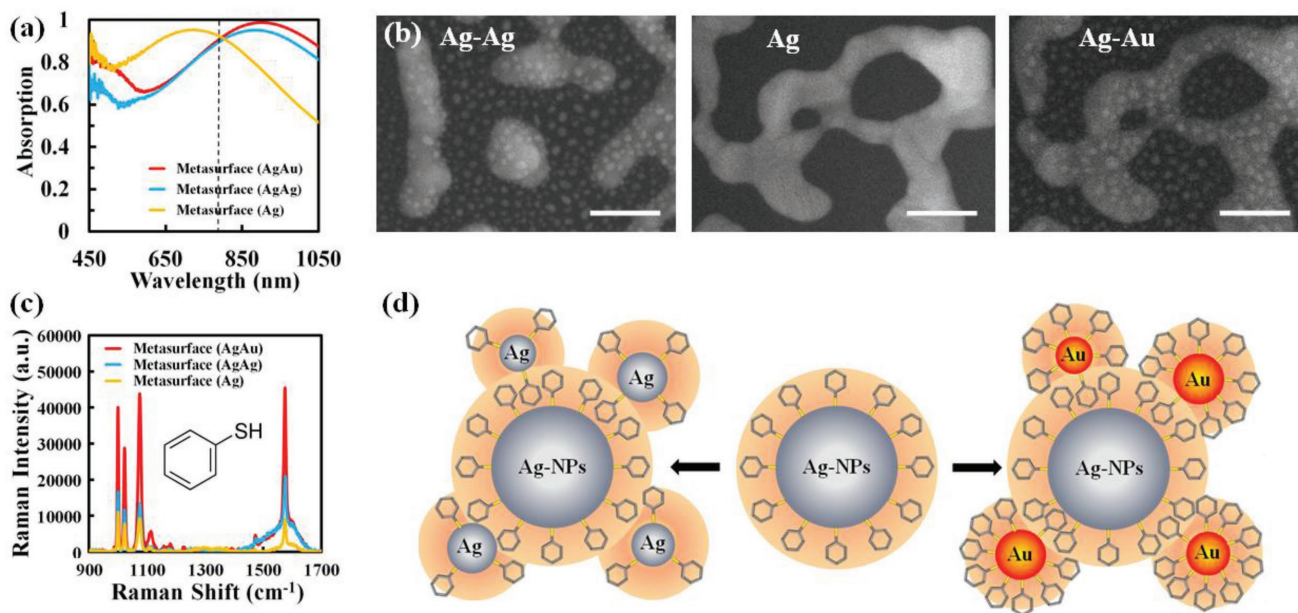
Figure 5. a) Absorption spectra of three metasurfaces: i.e., single-Ag (yellow curve), Ag–Ag (blue curve), and Ag–Au (red curve) metasurface chips. Black dashed line corresponds to the excitation wavelength of 785 nm. b) SEM images of top random Ag NPs before and after an extra 5 nm thick Ag or Au NP deposition. The scale bar is 100 nm. c) SERS spectra of BZT molecules on the metasurfaces with and without the second-step deposition. Inset: the chemical structure of BZT molecules. d) Schematic illustration of BZT molecular self-assemblies on the metasurfaces without (middle) and with the second-step Ag (left) or Au (right) NPs.

the three samples have similar optical absorption at the wavelength of 785 nm. As shown in Figure 5b, the second layer of Ag and Au NPs with similar sizes were inserted among the first layer Ag NPs, realizing smaller nanogaps. Their SERS signals were characterized under identical conditions using the excitation laser at 785 nm. As shown in Figure 5c, obvious Raman peaks at 1000, 1022, 1076, and 1576 cm^{-1} were observed, corresponding to signature "fingerprint" signals of BZT molecules. One can see that the Raman signal from the hybrid Ag–Au metasurface is stronger than the other two metasurfaces, which should be attributed to the stronger Au—S binding, as illustrated in Figure 5d. According to the second-order Møller–Plesset perturbation theory (MP2) and density functional theory (DFT),[46,47] the thiol—Au bond is stronger than that with Ag. In addition, the density of thiol chains of the SAM on Au surfaces is larger than that on Ag substrates.[50,51] In this case, more BZT molecules can adsorb to the surface of Au NPs with a better interaction with the localized field, resulting in the stronger SERS signal. The simulation was also performed to compare an Ag–Au metasurface with an Ag–Ag metasurface, confirming that the plasmonic coupling will not be affected much when the material composition changes from Ag–Au to Ag–Ag (see Section S3 in the Supporting Information). Therefore, the increased Raman signal from the hybrid Ag–Au metasurface should be attributed to the improved molecular binding to the surface.

3. Conclusions

In conclusion, we developed a scalable and cost-effective super-absorbing metasurface substrate that can localize electromagnetic field at edges of nanopatterns by introducing a second-step metal NP deposition process. This unique feature of localized field enhancement was validated through SERS sensing experiments. Intriguingly, since more hot spots were excited around extra small NPs over a given area, the uniformity of the spatial distribution of the localized field is improved, indicating the potential for quantitative sensing. Cocaine was selected as the sensing target to demonstrate the practical application of the proposed hybrid metasurface substrate in clinical and forensic trace analysis. Furthermore, the second-step coating of smaller Au NPs improved the reliability of the chip, which was demonstrated effective after one year shelf time in an ambient storage environment. The superior feature reported by this article paved the way toward more affordable and quantitative sensing using SERS technology. Particularly, due to stronger thiol—Au binding and higher density of thiol chains on Au surfaces, the proposed hybrid Ag–Au metasurface structure is promising to realize unique capabilities for sensing of bio/chemical molecules with thiol groups. More importantly, this efficient light trapping metasurface structure is completely lithography free, suitable for large area manufacturing including roll-to-roll processes. It will accelerate the development of low-cost high-performance SERS chips for portable Raman spectroscopy systems. This chip may lead to a widespread healthcare, security, anti-counterfeiting, and smart tool with far-reaching impacts on people's daily life, including biomedical diagnosis, security sensing, food/water safety monitoring, anti-counterfeiting, and

healthcare monitoring. In addition to providing a new understanding of broadband light trapping and field localization for sensing, this work also may open avenues toward new applications in energy harvesting, energy conversion, and surface-enhanced nonlinear optics.

4. Experimental Section

Metasurface Fabrication: The 1.5 × 1.5 cm^2 silicon wafers were sequentially sonicated in chromic acid, acetone, ethanol, and deionized water for 15 min. Next, a 150 nm thick Ag film, a 50 nm thick Al$_2$O$_3$ film, and a 12 nm thick Ag film were deposited on the wafer substrate using magnetron sputtering (Kurt J. Lesker PVD75). During the deposition, the pressure in the chamber was set to 3 × 10^{-6} Torr with no heating on the substrate. The deposition rate of Ag and Al$_2$O$_3$ was controlled by the sputter voltage and direct current power at 1 and 0.3 Å s^{-1}, respectively. Next, the top Ag film was transformed to isolated NPs by introducing a thermal annealing process at a temperature of 200 °C (i.e., Figure 2a) for 60 min. After the temperature in the chamber cooled down to the ambient temperature, a second layer of 5 nm thick Au film and Ag film were deposited at 1 Å s^{-1} on the samples, respectively, followed by thermal annealing at temperature of 150 °C for 60 min. To avoid a violet oxidization introduced by the high temperature, the argon was injected into the chamber to keep the pressure at 1.2 × 10^{-2} Torr during annealing processes.

Characterization: SEM images were taken using Zeiss CrossBeam Workstation system. The reflection/absorption spectra of metasurfaces were characterized using a microscopic Fourier transform infrared spectroscopy (Bruker, VETEX 70 + Hyperion 1000). Raman spectra were measured using a benchtop confocal Renishaw inVia Raman microscope equipped with a 785 nm laser. The power was set to 25 mW with the integration time of 1 s. A 20× objective lens was used to focus the excitation lasers onto the sample and collect the emitted Raman signals.

Enhancement Factor Calculation: The average enhancement factor, EF$_{ave}$, of the substrate is defined as EF$_{ave}$ = $(I_{SERS}/N_{SERS})/(I_{Raman}/N_{Raman})$, where I_{SERS} is the SERS intensity, I_{Raman} is the Raman intensity, N_{SERS} is the number of probed molecules in SERS, and N_{Raman} is the number of probed molecules in Raman measurements. Taking the excitation wavelength of 785 nm as an example, these four parameters can be calculated as below:

N_{SERS}—The scattering spectra were recorded in one acquisition with 1 s integration time in the spectral range of 900–1700 cm^{-1}. The laser beam was focused to be a Gaussian spot with the diameter of $\omega_0 = (4 \times \lambda)/(\pi \times NA)$, where NA is the numerical aperture of the objective lens (i.e., 0.4 in this experiment). In this case, the detection beam radius was estimated to be ≈1.25 µm, and the surface area of the beam was therefore ≈4.9 × 10^{-12} m^2. Assuming that the monolayer coverage density for BPE on the metasurface was 2 × 10^{13} molecules cm^{-2},[52,53] the number of probed molecules in SERS, N_{SERS}, was ≈9.8 × 10^5. It should be noted that the monolayer coverage density of BPE employed in the calculation was the largest number reported in previous literature. Lower densities would result in larger EFs.

N_{Raman}—A neat, liquid sample of the adsorbate molecule in a plastic cell was used as the Raman intensity standard. The probe volume of the confocal microscope with the 20× objective was estimated to be ≈7.5 pL (on the basis of 1/e^2 analysis[54,55]). Using the density of the liquid sample (i.e., 100 × 10^{-3} M, corresponding to ≈6.02 × 10^{22} molecules L^{-1}), the number of BPE molecules (N_{Raman}) contributing to the normal Raman signal measured from the standard was ≈4.5 × 10^{11}.

I_{Raman} and I_{SERS}—The intensities of the 1200 cm^{-1} peak from two metasurface chips with and without the second-step deposition process were used, as well as the regular Raman measurements. The excitation laser power and the acquisition time used in these two measurements were identical. I_{SERS} of two metasurface chips with and without the second-step deposition process were 16916.3 and 1070.8, respectively. I_{Raman} was 106.1.

Using these calculation results described above, one can obtain EF_{ave} of metasurface chips with and without the second-step deposition process, which were 7.3×10^7 and 4.7×10^6, respectively.

Supporting Information

Supporting Information is available from the Wiley Online Library or from the author.

Acknowledgements

Conflict of Interest

The authors declare no conflict of interest.

Keywords

[1] D. Cialla, A. März, R. Böhme, F. Theil, K. Weber, M. Schmitt, J. Popp, *Anal. Bioanal. Chem.* **2012**, *403*, 27.

[2] E. C. Le Ru, P. G. Etchegoin, *Annu. Rev. Phys. Chem.* **2012**, *63*, 65.

[3] R. S. Golightly, W. E. Doering, M. J. Natan, *ACS Nano* **2009**, *3*, 2859.

[4] K. C. Bantz, A. F. Meyer, N. J. Wittenberg, H. Im, Ö. Kurtuluş, S. H. Lee, N. C. Lindquist, S. H. Oh, C. L. Haynes, *Phys. Chem. Chem. Phys.* **2011**, *13*, 11551.

[5] J. A. Schuller, E. S. Barnard, W. Cai, Y. C. Jun, J. S. White, M. L. Brongersma, *Nat. Mater.* **2010**, *9*, 193.

[6] L. Novotny, N. Van Hulst, *Nat. Photonics* **2011**, *5*, 83.

[7] V. Giannini, A. I. Fernández-Domínguez, Y. Sonnefraud, T. Roschuk, R. Fernández-García, S. A. Maier, *Small* **2010**, *6*, 2498.

[8] J. M. Nam, J. W. Oh, H. Lee, Y. D. Suh, *Acc. Chem. Res.* **2016**, *49*, 2746.

[9] H. Im, K. C. Bantz, N. C. Lindquist, C. L. Haynes, S. H. Oh, *Nano Lett.* **2010**, *10*, 2231.

[10] Z. Zhu, B. Bai, H. Duan, H. Zhang, M. Zhang, O. You, Q. Li, Q. Tan, J. Wang, S. Fan, G. Jin, *Small* **2014**, *10*, 1603.

[11] S. W. Lee, K. S. Lee, J. Ahn, J. J. Lee, M. G. Kim, Y. B. Shin, *ACS Nano* **2011**, *5*, 897.

[12] J. Qi, P. Motwani, M. Gheewala, C. Brennan, J. C. Wolfe, W.-C. Shih, *Nanoscale* **2013**, *5*, 4105.

[13] L. Zhang, X. Lang, A. Hirata, M. Chen, *ACS Nano* **2011**, *5*, 4407.

[14] K. Liu, X. Zeng, S. Jiang, D. Ji, H. Song, N. Zhang, Q. Gan, *Nanoscale* **2014**, *6*, 5599.

[15] N. Zhang, Z. Dong, D. Ji, H. Song, X. Zeng, Z. Liu, S. Jiang, Y. Xu, A. A. Bernussi, W. Li, Q. Gan, *Appl. Phys. Lett.* **2016**, *108*, 091105.

[16] N. Zhang, K. Liu, Z. Liu, H. Song, X. Zeng, D. Ji, A. Cheney, S. Jiang, Q. Gan, *Adv. Mater. Interfaces* **2015**, *2*, 1500142.

[17] V. Kumar, S. K. Yadav, *J. Chem. Technol. Biotechnol.* **2009**, *84*, 151.

[18] http://www.silmeco.com/products/sers-substrate-serstrate/ (accessed: January 2018).

[19] http://www.atoid.com/shop/sersgold/ (accessed: January 2018).

[20] Z. A. Nima, Y. R. Davletshin, F. Watanabe, K. M. Alghazali, J. C. Kumaradas, A. S. Biris, *RSC Adv.* **2017**, *7*, 53164.

[21] H. J. Yin, Z. Y. Chen, Y. M. Zhao, M. Y. Lv, C. A. Shi, Z. L. Wu, X. Zhang, L. Liu, M. L. Wang, H. J. Xu, *Sci. Rep.* **2015**, *5*, 14502.

[22] S. Ayas, H. Güner, B. Türker, O. O. Ekiz, F. Dirisaglik, A. K. Okyay, A. Dâna, *ACS Nano* **2012**, *6*, 6852.

[23] T. Søndergaard, S. M. Novikov, T. Holmgaard, R. L. Eriksen, J. Beermann, Z. Han, K. Pedersen, S. I. Bozhevolnyi, *Nat. Commun.* **2012**, *3*, 969.

[24] H. Song, L. Guo, Z. Liu, K. Liu, X. Zeng, D. Ji, N. Zhang, S. Jiang, Q. Gan, *Adv. Mater.* **2014**, *26*, 2737.

[25] H. Song, N. Zhang, J. Duan, Z. Liu, J. Gao, M. H. Singer, D. Ji, A. R. Cheney, X. Zeng, B. Chen, S. Jiang, Q. Gan, *Adv. Opt. Mater.* **2017**, *5*, 1700166.

[26] N. Zhang, Z. Ji, A. Cheney, H. Song, D. Ji, X. Zeng, B. Chen, T. Zhang, A. Cartwright, K. Shi, Q. Gan, *Sci. Rep.* **2017**, *7*, 4346.

[27] N. G. Greeneltch, M. G. Blaber, A. I. Henry, G. C. Schatz, R. P. Van Duyne, *Anal. Chem.* **2013**, *85*, 2297.

[28] A. Kim, F. S. Ou, D. A. A. Ohlberg, M. Hu, R. S. Williams, Z. Li, *J. Am. Chem. Soc.* **2011**, *133*, 8234.

[29] V. Liberman, C. Yilmaz, T. M. Bloomstein, S. Somu, Y. Echegoyen, A. Busnaina, S. G. Cann, K. E. Krohn, M. F. Marchant, M. Rothschild, *Adv. Mater.* **2010**, *22*, 4298.

[30] B. Sharma, M. F. Cardinal, S. L. Kleinman, N. G. Greeneltch, R. R. Frontiera, M. G. Blaber, G. C. Schatz, R. P. Van Duyne, *MRS Bull.* **2013**, *38*, 615.

[31] N. Nuntawong, P. Eiamchai, B. Wong-ek, M. Horprathum, K. Limwichean, V. Patthanasettakul, P. Chindaudom, *Vacuum* **2013**, *88*, 23.

[32] L. Bachenheimer, R. Scherzer, P. Elliott, S. Stagon, L. Gasparov, H. Huang, *Sci. Rep.* **2017**, *7*, 16282.

[33] B. Zhang, Y. Shi, H. Chen, Q. Zhu, F. Lu, Y. Li, *Anal. Chim. Acta* **2018**, *997*, 35.

[34] L. Yang, Y. Chen, H. Li, L. Luo, Y. Zhao, H. Zhang, Y. Tian, *Anal. Methods* **2015**, *7*, 6520.

[35] B. Zhang, X. Yin, D. Zhen, W. Gu, Y. Liu, Q. Cai, *New J. Chem.* **2017**, *41*, 13968.

[36] C. A. F. Penido, M. T. T. Pacheco, I. K. Lednev, L. Silveira, *J. Raman Spectrosc.* **2016**, *47*, 28.

[37] C. Muehlethaler, M. Leona, J. R. Lombardi, *Anal. Chem.* **2015**, *88*, 152.

[38] S. Farquharson, C. Shende, A. Sengupta, H. Huang, F. Inscore, *Pharmaceutics* **2011**, *3*, 425.

[39] E. Horvath, J. Mink, J. Kristof, *Mikrochim. Acta* **1997**, *14*, 745.

[40] B. Sägmüller, B. Schwarze, G. Brehm, G. Trachta, S. Schneider, *J. Mol. Struct.* **2003**, *661*, 279.

[41] J. C. Carter, W. E. Brewer, S. M. Angel, *Appl. Spectrosc.* **2000**, *54*, 1876.

[42] J. Chen, J. Jiang, X. Gao, G. Liu, G. Shen, R. Yu, *Chem. - Eur. J.* **2008**, *14*, 8374.

[43] F. Wang, R. G. Widejko, Z. Yang, K. T. Nguyen, H. Chen, L. P. Fernando, K. A. Christensen, J. N. Anker, *Anal. Chem.* **2012**, *84*, 8013.

[44] W. Hasi, S. Lin, X. Lin, X. Lou, F. Yang, D. Lin, Z. Lu, *Anal. Methods* **2014**, *6*, 9547.

[45] W. Tao, A. Zhao, H. Sun, Z. Gan, M. Zhang, D. Li, H. Guo, *RSC Adv.* **2014**, *4*, 3487.

[46] A. H. Pakiari, Z. Jamshidi, *J. Phys. Chem. A* **2010**, *114*, 9212.

[47] J. Granatier, M. Urban, A. J. Sadlej, *J. Phys. Chem. A* **2007**, *111*, 13238.

[48] J. Ruff, J. Steitz, A. Buchkremer, M. Noyong, H. Hartmann, A. Besmehn, U. Simon, *J. Mater. Chem. B* **2016**, *4*, 2828.

[49] L. J. Wan, M. Terashima, H. Noda, M. Osawa, *J. Phys. Chem. B* **2000**, *104*, 3563.

[50] K. V. G. K. Murty, M. Venkataramanan, T. Pradeep, *Langmuir* **1998**, *14*, 5446.

[51] J. C. Love, D. B. Wolfe, R. Haasch, M. L. Chabinyc, K. E. Paul, G. M. Whitesides, R. G. Nuzzo, *J. Am. Chem. Soc.* **2003**, *125*, 2597.

[52] X. Yang, N. Ileri, C. C. Larson, T. C. Carlson, J. A. Britten, A. S. P. Chang, C. Gu, T. C. Bond, *Opt. Express* **2012**, *20*, 24819.

[53] A. Gutes, I. Laboriante, C. Carraro, R. Maboudian, *J. Phys. Chem. C* **2009**, *113*, 16939.

[54] C. L. Haynes, R. P. Van Duyne, *J. Phys. Chem. B* **2003**, *107*, 7426.

[55] C. M. Whelan, M. R. Smyth, C. J. Barnes, *Langmuir* **1999**, *15*, 116.